

Gyrokinetic particle simulation of beta-induced Alfvén eigenmode

H. S. Zhang,^{1,2} Z. Lin,^{2,a)} I. Holod,² X. Wang,^{3,2} Y. Xiao,² and W. L. Zhang^{4,2}

¹*Fusion Simulation Center and State Key Laboratory of Nuclear Physics and Technology, Peking University, Beijing 100871, China*

²*Department of Physics and Astronomy, University of California, Irvine, Irvine, California 92697, USA*

³*Institute for Fusion Theory and Simulation, Zhejiang University, Hangzhou 310027, China*

⁴*CAS Key Laboratory of Plasma Physics, University of Science and Technology of China, Hefei, Anhui 230026, China*

(Received 17 August 2010; accepted 17 September 2010; published online 9 November 2010)

The beta-induced Alfvén eigenmode (BAE) in toroidal plasmas is studied using global gyrokinetic particle simulations. The BAE real frequency and damping rate measured in the initial perturbation simulation and in the antenna excitation simulation agree well with each other. The real frequency is slightly higher than the ideal magnetohydrodynamic (MHD) accumulation point frequency due to the kinetic effects of thermal ions. Simulations with energetic particle density gradient show exponential growth of BAE with a growth rate sensitive to the energetic particle temperature and density. The nonperturbative contributions by energetic particles modify the mode structure and reduce the frequency relative to the MHD theory. The finite Larmor radius effects of energetic particles reduce the BAE growth rate. Benchmarks between gyrokinetic particle simulation and hybrid MHD-gyrokinetic simulation show good agreement in BAE real frequency and mode structure. © 2010 American Institute of Physics. [doi:10.1063/1.3498761]

I. INTRODUCTION

In tokamak experiments, the Alfvén eigenmodes, such as the toroidal Alfvén eigenmode¹ (TAE) and β -induced Alfvén eigenmode (BAE),^{2,3} are a major concern because they can be easily destabilized by energetic particles through wave-particle interaction and can cause the loss of the energetic particles. The BAE frequency is around the β -induced gap of the Alfvén continuum^{4,5} in the toroidal geometry, which is on the order of the thermal ion transit frequency.⁶ Thus, the BAE has strong interaction with both thermal ions and energetic particles.⁷ Theoretically, the BAE frequency is due to the finite compressibility induced by the geodesic curvature of the equilibrium magnetic field, together with the plasma pressure.^{5,6,8} The BAE is observed in various tokamaks with energetic particles,^{2,9} strong tearing mode activity,^{10–13} and ion cyclotron resonant heating.¹⁴ Several theories have been proposed to explain the excitation of oscillations with the BAE frequency, such as Alfvén eigenmode,⁴ kinetic ballooning mode (KBM),¹⁵ energetic particle mode,^{16–18} hybrid mode between Alfvénic and KBM,¹⁹ and magnetic island-induced free energy.²⁰ The BAE damping effect is also investigated through numerical solution.²¹ Meanwhile, the relation between BAE and the electrostatic geodesic acoustic mode²² (GAM) have also been discussed,^{7,23–25} which shows that the kinetic theory is needed to correctly describe the BAE physics.

Although there have been extensive works on BAE through experimental and theoretical studies, few works have been reported on BAE simulations²⁶ and nonlinear studies. In this work, using the electromagnetic gyrokinetic toroidal code (GTC),^{27,28} we carry out gyrokinetic particle

simulation of the BAE for the first time. GTC has been successfully applied to the simulations of magnetohydrodynamic (MHD) modes such as TAE,²⁹ reversed shear Alfvén eigenmode (RSAE),³⁰ and GAM.^{31,32} Here, we successfully excite the BAE in GTC simulations both by an antenna excitation and by energetic particle density gradient. The antenna excitation method, which is also used in tokamak experiments,^{33–35} enables us to accurately measure the BAE frequency, damping rate, and mode structure for verifying GTC simulation of the BAE excited by the energetic particles. We find that the BAE frequency at small q (q is the safety factor) is slightly higher than the BAE accumulation point frequency and also higher than the theoretical prediction.^{8,23,24,26} The energetic particle excitation shows an exponential growth of the BAE. Comparisons between the antenna excitation and the energetic particle excitation show that the BAE frequency excited by the energetic particles has a small downshift. The BAE frequency in both antenna and energetic particle excitation varies slightly with the plasma β and $k_{\theta}\rho_i$ (β is the ratio between plasma pressure and magnetic pressure and k_{θ} and ρ_i are the poloidal wave number and thermal ion Larmor radius, respectively). The BAE growth rate in the energetic particle excitation is sensitive to the energetic particle temperature and density. Furthermore, we find that nonperturbative contributions by the energetic particles modify the BAE mode structure and frequency relative to the ideal MHD theory. The finite Larmor radius effects of the energetic particles reduce the BAE growth rate. Benchmarks between GTC and a hybrid MHD-gyrokinetic code XHMGC^{26,36} show that the results of the two codes agree well on the frequency and mode structure, which provides a further verification of the gyrokinetic particle simulation of BAE.

^{a)}Author to whom correspondence should be addressed. Electronic mail: zhihongl@uci.edu.

The paper is organized as follows: GTC formulation is presented in Sec. II. In Sec. III, BAE excitation by antenna and energetic particles are investigated. Benchmarks between GTC and XHMGC are shown in Sec. IV. Section V is the summary.

II. GTC FORMULATION FOR BAE SIMULATION

In the GTC formulation, both thermal and energetic ions are described by the nonlinear gyrokinetic equation³⁷

$$(\partial_t + \dot{\mathbf{X}} \cdot \nabla + \dot{v}_{\parallel} \partial_{\parallel}) f_{\alpha}(\mathbf{X}, \mu, v_{\parallel}, t) = 0, \quad (1)$$

$$\dot{\mathbf{X}} = v_{\parallel} \frac{\mathbf{B}}{B_0} + \mathbf{v}_E + \mathbf{v}_c + \mathbf{v}_g, \quad (2)$$

$$\dot{v}_{\parallel} = - \frac{\mathbf{B}^*}{m_{\alpha} B_0} \cdot (\mu \nabla B_0 + Z_{\alpha} \nabla \delta \phi) - \frac{Z_{\alpha}}{m_{\alpha} c} \partial_t \delta A_{\parallel}. \quad (3)$$

Here, all perturbed quantities (δA_{\parallel} , $\delta \phi$) are gyro-averaged. α stands for thermal ions (i) or energetic particles (f). Z_{α} and m_{α} are the charge and mass of species α , respectively. $\mathbf{B} = \mathbf{B}_0 + \delta \mathbf{B}$, where \mathbf{B}_0 and $\delta \mathbf{B}$ are the equilibrium part and the perturbed part of the magnetic field, respectively, $\mathbf{B}^* = \mathbf{B}_0 + B_0 v_{\parallel} / \Omega_{\alpha} \nabla \times \mathbf{b}_0 + \delta \mathbf{B}$, and $\delta \mathbf{B} = \nabla \times (\delta A_{\parallel} \mathbf{b}_0)$. Ω_{α} is the cyclotron frequency of species α . The $\mathbf{E} \times \mathbf{B}$ drift \mathbf{v}_E , curvature drift \mathbf{v}_c and grad- \mathbf{B} drift \mathbf{v}_g are given by

$$\mathbf{v}_E = \frac{c \mathbf{b}_0 \times \nabla \delta \phi}{B_0}, \quad (4)$$

$$\mathbf{v}_c = \frac{v_{\parallel}^2}{\Omega_{\alpha}} \nabla \times \mathbf{b}_0, \quad (5)$$

$$\mathbf{v}_g = \frac{\mu}{m_{\alpha} \Omega_{\alpha}} \mathbf{b}_0 \times \nabla B_0. \quad (6)$$

Electrons are treated using the fluid-kinetic hybrid electron model.^{28,38–40} In the lowest order, electron response is adiabatic and can be described by the fluid continuity equation by taking moments of Eq. (1) in the drift-kinetic limit ($k_{\perp} \rho_e = 0$)

$$\begin{aligned} & -i\omega \delta n_e + \mathbf{B}_0 \cdot \nabla \left(\frac{n_0 \delta v_{e\parallel}}{B_0} \right) \\ & = \frac{1}{m_e \Omega_e} \mathbf{b}_0 \times \nabla (\delta P_{e\parallel} + \delta P_{e\perp}) \cdot \frac{\nabla B_0}{B_0} - B_0 \mathbf{v}_E \cdot \nabla \left(\frac{n_0}{B_0} \right) \\ & + n_0 \mathbf{v}_E \cdot \frac{\nabla B_0}{B_0}. \end{aligned} \quad (7)$$

Here, $\delta P_{e\parallel} = \int m v_{\parallel}^2 \delta f_e dv$ and $\delta P_{e\perp} = \int \mu B_0 \delta f_e dv$. According to Eqs. 19 and 20 of Ref. 28, $\delta P_{e\parallel} = \delta P_{e\perp} = n_0 e \delta \phi_{\text{eff}}$ in the lowest order for uniform and isotropic plasmas. Here, n_0 is the background electron density and $\delta \phi_{\text{eff}}$ is the effective potential representing the parallel electric field, i.e. $\delta E_{\parallel} = -\mathbf{b}_0 \cdot \nabla \delta \phi_{\text{eff}}$. Meanwhile,

$$\frac{\partial \delta A_{\parallel}}{c \partial t} = \mathbf{b}_0 \cdot \nabla \delta \phi - \delta E_{\parallel}. \quad (8)$$

For uniform background plasma, $n_0 e \delta \phi_{\text{eff}} = \delta n_e T_e$ in the lowest order (δn_e is the perturbed electron density). Nonlinear terms are dropped in Eq. (7) for the linear simulation of BAE. The system is closed with the gyrokinetic Poisson's equation⁴¹

$$\frac{Z_i^2 n_i}{T_i} (\delta \phi - \delta \tilde{\phi}) = \sum_{\alpha=e,i,f} Z_{\alpha} \delta n_{\alpha} \quad (9)$$

and the parallel Ampère's law

$$\frac{4\pi}{c} e \delta v_{e\parallel} = \frac{4\pi}{c} (Z_i \delta v_{i\parallel} + Z_f \delta v_{f\parallel}) - \nabla_{\perp}^2 \delta A_{\parallel}, \quad (10)$$

where $\delta \tilde{\phi}$ is defined as the second gyrophase-averaged potential.⁴²

Next, we show that the system of Eqs. (1)–(10) can recover the ideal MHD results in the long wavelength limit ($k_{\perp} \rho_i \ll 1$, $\rho_i = v_i / \Omega_i$) and when ignoring all kinetic effects. In this case, $\delta E_{\parallel} = -\mathbf{b}_0 \cdot \nabla \delta \phi - \partial \delta A_{\parallel} / c \partial t = 0$ and Eq. (9) becomes

$$\nabla_{\perp} \cdot \left(\frac{\nabla_{\perp} \delta \phi}{v_A^2} \right) = - \frac{4\pi}{c^2} (-e \delta n_e + Z_i \delta n_i + Z_f \delta n_f), \quad (11)$$

where $v_A = B / \sqrt{4\pi n_i m_i}$ is the Alfvén velocity. By using Eq. (7) for all species and Eq. (10), we can get,

$$\begin{aligned} & \omega^2 \nabla_{\perp} \cdot \left(\frac{\nabla_{\perp} \delta \phi}{v_A^2} \right) - i\omega \frac{4\pi}{c} \nabla \cdot \left(\frac{\mathbf{b}_0}{B_0} \times \nabla \cdot \delta \mathbf{P} \right) \\ & = - \mathbf{B}_0 \cdot \nabla \left[\frac{1}{B_0} \nabla^2 (\mathbf{b}_0 \cdot \nabla \delta \phi) \right], \end{aligned} \quad (12)$$

with $\delta \mathbf{P} = \delta \mathbf{P}_e + \delta \mathbf{P}_i + \delta \mathbf{P}_f$ and $\delta \mathbf{P}_{\alpha} = \delta P_{\alpha\parallel} \mathbf{b}_0 \mathbf{b}_0 + \delta P_{\alpha\perp} (\mathbf{I} - \mathbf{b}_0 \mathbf{b}_0)$ in the drift-kinetic limit. The charge neutrality $\sum_{\alpha} Z_{\alpha} n_{\alpha 0} = 0$ and $\nabla \times \mathbf{B}_0 \approx \mathbf{0}$ are used in the derivation, i.e., equilibrium current is neglected. We note that Eq. (12) recovers the ideal MHD equations with pressure term and is consistent with the formulation of XHMGC.²⁶

Finally, we derive the BAE linear dispersion relation only considering the fluid electron pressure for simplicity. In the toroidal geometry, we can decompose perturbed quantities in n and m harmonic (m and n are poloidal and toroidal mode number, respectively), i.e., $\delta \phi(r, \theta, \zeta) = \delta \phi(\hat{r}) \exp[i(n\zeta - m\theta)]$ (θ and ζ are the poloidal and toroidal angle, respectively). In uniform plasmas, there is no diamagnetic drift in Eq. (7). We also drop the δv_{\parallel} term because $k_{\parallel} = 0$ for the BAE. In this case, only the $E \times B$ drift is considered and the continuity equation is reduced to

$$\frac{\partial \delta n_e}{\partial t} = -n_0 \nabla \cdot \frac{c \nabla \delta \hat{\phi} \times \mathbf{B}_0}{B_0^2}. \quad (13)$$

Since $\delta P_e = n_0 e \delta \phi_{\text{eff}} = \delta n_e T_e$ and using Eq. (13), the pressure term in Eq. (12) can be written as

$$\begin{aligned}
& -i\omega \frac{4\pi}{c} \nabla \cdot \left(\frac{\mathbf{b}_0}{B_0} \times \nabla \delta P_e \right) \\
& = -n_0 T_e \nabla \left[\nabla \delta \hat{\phi} \cdot \nabla \times \left(\frac{\mathbf{B}_0}{B_0^2} \right) \right] \cdot \nabla \times \left(\frac{\mathbf{B}_0}{B_0^2} \right). \quad (14)
\end{aligned}$$

After ignoring the $O(\epsilon^2/q^2)$ term and doing flux surface average, Eq. (12) becomes

$$\begin{aligned}
& \frac{1}{r} \frac{d}{dr} r \left(\frac{\omega^2}{v_A^2} - k_{\parallel}^2 - \frac{2C_s^2}{v_A^2 R_0^2} \right) \frac{d}{dr} \delta \hat{\phi} - \frac{m^2}{r^2} \left(\frac{\omega^2}{v_A^2} - k_{\parallel}^2 - \frac{2C_s^2}{v_A^2 R_0^2} \right) \delta \hat{\phi} \\
& - \frac{k_{\parallel}}{r} \frac{d(k'_{\parallel} r)}{dr} \delta \hat{\phi} = 0. \quad (15)
\end{aligned}$$

Here, $C_s^2 = T_e/m_i$ and $k_{\parallel} = (n-m/q)/R_0$. Thus, the local dispersion relation for the Alfvén continuum with plasma pressure effect can be given by

$$\frac{\omega^2}{v_A^2} - k_{\parallel}^2 - \frac{2C_s^2}{v_A^2 R_0^2} = 0. \quad (16)$$

When $k_{\parallel} = (n-m/q)/R_0 = 0$, the Alfvén continuum reaches the accumulation point with a frequency defined as the BAE frequency, which is the same as GAM frequency. More generally, the pressure term contains both the fluid electron and kinetic ion pressure and the frequency is given by

$$\omega_{\text{BAE}} = \sqrt{\left(\frac{7}{2} T_i + 2T_e \right) / (m_i R_0^2)}. \quad (17)$$

Detailed derivations of the BAE frequency are presented in Refs. 6, 23, and 24.

III. GTC SIMULATION OF BAE EXCITATION

In this simulation, we use $a/R_0 = 0.3$ (a and R_0 are tokamak minor and major radius, respectively). Protons are used as the background ions while T_e is set to be 0 by letting $\delta E_{\parallel} = 0$. In this case, the Alfvén accumulation point frequency is $\omega_{\text{BAE}} = \sqrt{7T_i / (2m_i R_0^2)} \approx 1.32v_i / R_0$ with $v_i = \sqrt{2T_i / m_i}$. The background plasma is uniform with $\beta = 4\pi n_0 (T_i + T_e) / B_0^2 = 0.0072$. The $q=2$ mode rational surface locates at $\epsilon = r/R_0 = 0.15$ (r is the local minor radius). The $n=4$ mode is selected in the linear simulation. Since the BAE is a $k_{\parallel} \approx 0$ mode, we additionally apply a poloidal filter to keep only the $m=nq$ and $m=nq \pm 1$ harmonics to avoid the high frequency noise. The wavelength of the BAE is $k_{\theta} \rho_i = 0.09$ and 32 grid points per wavelength are used in the simulation.

First, an artificial antenna³⁰ is used to excite the BAE. Finite Larmor radius effects are ignored first. Figure 1(a) is the time evolution of the ($n=4$, $m=8$) BAE mode excited with an antenna frequency $\omega_{\text{ant}} = 1.67v_i / R_0$. The mode amplitude saturates quickly due to the large damping rate. Figure 1(b) is the poloidal mode structure of the electrostatic potential. The $m=8$ harmonic is well formed around the $q=2$ mode rational surface. According to the driven resonant cavity theory,⁴³ if a damped eigenmode is excited by an antenna, the saturated intensity of the eigenmode is given by

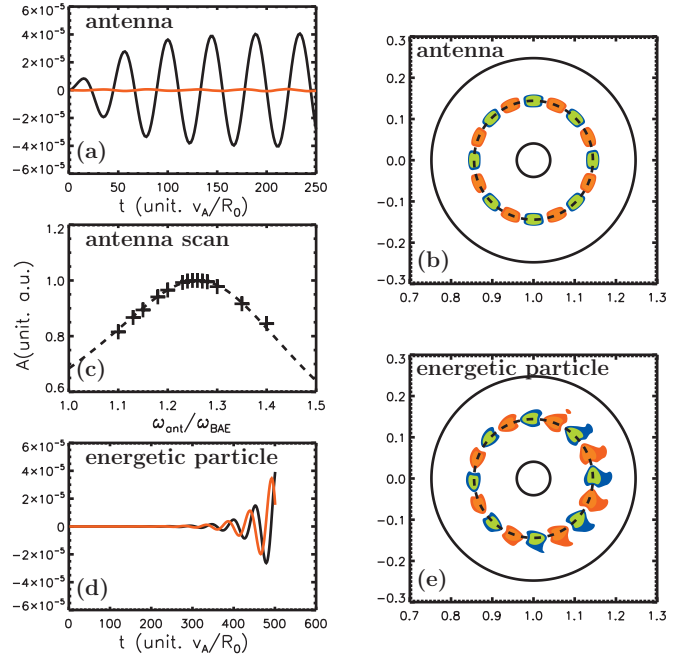


FIG. 1. (Color) (a) Time evolution and (b) poloidal mode structure of the BAE excited by antenna with $\omega_{\text{ant}} = 1.67v_i / R_0$. (c) Saturated amplitude vs antenna frequency. The dashed line is the numerical fitting by Eq. (18). (d) and (e) are the time evolution and poloidal mode structure of the BAE excited by energetic particles. In (a) and (d), the black line is the real part and the red line is the imaginary part. In (b) and (e), the dashed circle is the $q=2$ surface.

$$A^2 \propto \frac{1}{(\omega_0^2 + \gamma^2 - \omega_{\text{ant}}^2)^2 + 4\gamma^2 \omega_{\text{ant}}^2}. \quad (18)$$

Here, A^2 is the normalized saturated intensity and ω_0 and γ are the real frequency and damping rate of the eigenmode, respectively. This method is also used in tokamak experiments to measure the mode frequency and damping rate.^{34,35}

Figure 1(c) is the antenna frequency scan of the saturated BAE amplitude. The numerical fitting of the simulation results by Eq. (18) shows that the eigen frequency and damping rate are $1.65v_i / R_0$ and $-0.36v_i / R_0$, respectively. The observed frequency is about 25% higher than ω_{BAE} and also about 15% higher than the theoretical prediction in Refs. 8, 23, 24, and 26. We note that these theories are based on the assumption of small ϵ and large q . The large damping rate suggests that the thermal ion damping effect is strong because the BAE frequency is close to the thermal ion transit frequency $\omega_i = v_i / (qR_0)$.

Next, the energetic particle density gradient is used to excite the BAE. We also use protons as the energetic particles. The maximum density gradient $R/L_{n_f} \approx 46$ is located at the $q=2$ and $\epsilon=0.15$ surface. The energetic particles have a Maxwellian distribution with $T_f = 16T_i$ and $n_f = 0.01n_0$, respectively. In this case, the energetic particle $k_{\theta} \rho_E = 0.36$. The drift-kinetic limit is taken first for simplicity and for comparison with the gyrokinetic simulation with finite Larmor radius effects. Figure 1(d) is the time evolution of the BAE mode. Different from Fig. 1(a), the energetic particle excited BAE mode grows exponentially. The imaginary part of the mode is $\pi/2$ leading the real part in phase, which means that

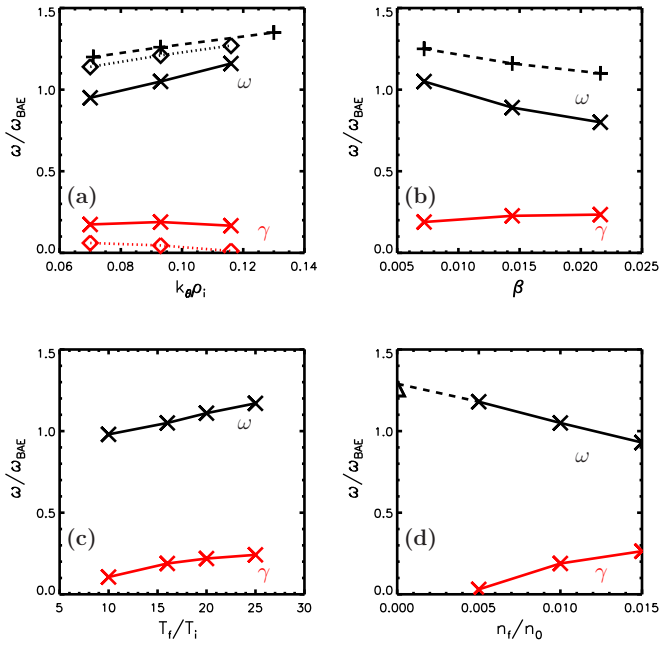


FIG. 2. (Color online) [(a) and (b)] Wave vector $k_{\theta\rho_i}$ scan and plasma β scan of the BAE frequency excited by antenna (“+”) and energetic particles (“×” and “◇”). × and ◇ correspond to energetic particle density gradient $R_0/L_{nj}=46$ and $R_0/L_{nj}=25$, respectively. [(c) and (d)] T_r scan and n_f scan of the BAE frequency. The “△” in (d) is the antenna excited BAE frequency. The gray lines (or red lines online) are the growth rate. The finite Larmor radius effects are ignored in all these simulations.

this wave is a traveling wave and propagates in the fast ion diamagnetic direction. The mode frequency and growth rate are $1.40v_i/R_0$ and $0.25v_i/R_0$, respectively. The frequency is slightly lower than the antenna result due to the nonperturbative contributions by energetic particles. Comparing the poloidal mode structure of the antenna excitation case [Fig. 1(b)] and the energetic particle excitation case [Fig. 1(e)], the mode structure in Fig. 1(b), which corresponds to the MHD theory, is slightly different from Fig. 1(e), since the energetic particles are treated nonperturbatively, which breaks the radial symmetry. The gyrokinetic simulation with finite Larmor radius effects is also carried out with the same parameters and the frequency and growth rate are $1.44v_i/R_0$ and $0.19v_i/R_0$, respectively. The difference between the gyrokinetic and the drift-kinetic simulations for the BAE linear growth rate is due to finite Larmor radius effects.

We further find that BAE frequency slightly depends on the wave vector $k_{\theta\rho_i}$ and plasma β in the drift-kinetic limit. Figures 2(a) and 2(b) show the $k_{\theta\rho_i}$ scan and the β scan for the BAE frequency. We can see that the BAE frequency in our simulation increases as $k_{\theta\rho_i}$ increases or as β decreases in both antenna excitation and energetic particle excitation. The wave vector dependence is due to finite Larmor radius and the finite orbit width effects. Furthermore, we find that the energetic particle excited BAE frequency is always downshifted compared to the antenna cases due to the nonperturbative contributions from the energetic particle. As we can see from Fig. 2(a), the larger the density gradient, the stronger the frequency downshift. Meanwhile, the growth rate changes little with respect to $k_{\theta\rho_i}$ and β but increases strongly with larger density gradient. Different energetic par-

ticle temperature and density ratio are also used; we find that the BAE frequency increases as T_f increases or as n_f decreases. However, the growth rate is always enhanced as we increase T_f or n_f . In Fig. 2(d), we extrapolate the frequency to $n_f=0$, where there is no energetic particle pressure, and find that the frequency is quite close to the antenna excitation results. From these figures we can see that the growth rate of the BAE excited by the energetic particle is related to the energetic particle drives (T_f , n_f , etc). Increasing either R_0/L_{nj} , T_f , or n_f can enhance the excitation of the BAE.

IV. VERIFICATION OF GYROKINETIC SIMULATION OF BAE

Since this work is the first gyrokinetic particle simulation of the BAE, we verify the GTC simulation by benchmarking with a hybrid MHD-gyrokinetic code XHMGC^{26,36} using the same parameters. In the following subsections, we compare the BAE results between GTC and XHMGC using initial perturbation, antenna excitation, and energetic particle excitation, separately. The simulation parameters in both codes are $a/R_0=0.1$ and $\beta=0.0072$. The $q=3$ surface is located at $\epsilon=0.05$. The $n=3$ toroidal mode is selected with the $m=nq$ and $m=nq \pm 1$ harmonics kept in the poloidal direction. Electron temperature is set to be $T_e=0$ and drift-kinetic simulations are carried out for thermal and energetic ions. There is a small difference in the geometry: GTC uses a concentric circular cross-section in the current simulation, while XHMGC has a Shafranov shift. GTC neglects the equilibrium current but XHMGC keeps it. Numerical convergence in GTC simulation has also been demonstrated.

A. BAE simulation with an initial perturbation

In the initial perturbation simulation, a harmonic of ($n=3$, $m=9$) electron density perturbation is initiated around the $q=3$ surface. Figure 3 is the BAE simulations by GTC and XHMGC. This mode has a frequency of $\omega=1.47v_i/R_0$ and a finite damping rate $\gamma=-0.07v_i/R_0$ in the GTC simulation, while $\omega=1.42v_i/R_0$ and $\gamma=-0.15v_i/R_0$ in the XHMGC simulation. The frequency in the two codes agrees very well and also agrees with the theoretical result,^{6,7} which can be expected in the large q and small ϵ limit. The damping rate in GTC is smaller than XHMGC, which may be due to the different equilibrium current and geometry used in the two codes and the additional numerical viscosity and resistivity in XHMGC. The final mode structures of GTC [Fig. 3(c)] and XHMGC [Fig. 4(d)] agree very well and are almost the same as the initial state. There is no phase mixing in this region, which means that this is an eigenmode rather than a quasimode at the accumulation point of the Alfvén continuum. The existence of the eigenmode may be due to the kinetic effects, which move the BAE frequency slightly away from the accumulation point.²⁶

B. BAE excitation by antenna

Antenna frequency scan is also carried out to find the BAE frequency and damping rate in both GTC and XHMGC simulation. Figure 4(a) is the time evolution of the

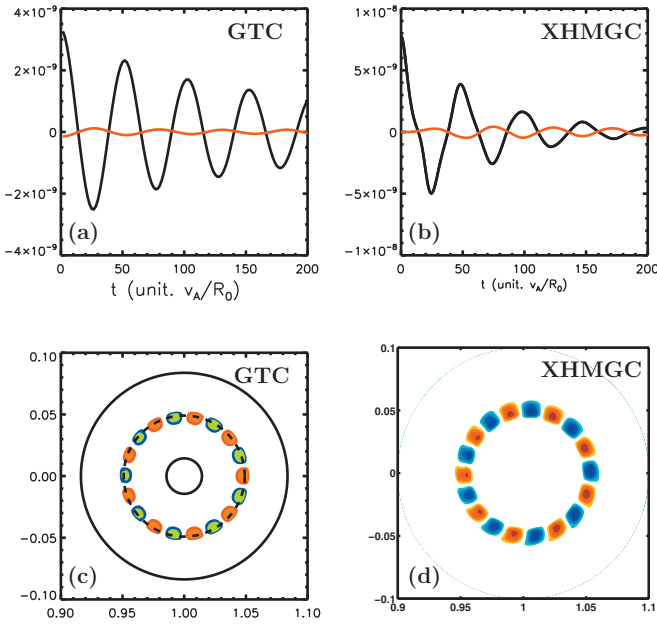


FIG. 3. (Color) BAE simulations with an initial perturbation for the time evolution of the $(n=3, m=9)$ mode (upper panels) and final poloidal mode structures (lower panels). GTC and xHMGC simulation results are on the left and right hand sides, respectively. In (a) and (b), the black and red lines are the real and imaginary parts, respectively. The dashed line in (c) is the $q=3$ surface.

$(n=3, m=9)$ mode with antenna frequency $\omega_{\text{ant}}=1.46v_i/R_0$ in the GTC simulation. We can see that the mode first grows linearly and then saturates slower than the $q=2$ case in Fig. 1(b) because the damping is weaker for the $q=3$ case. Figure 4(b) shows the frequency scan of the saturated BAE amplitude. The numerical fitting by Eq. (18) finds that the fre-

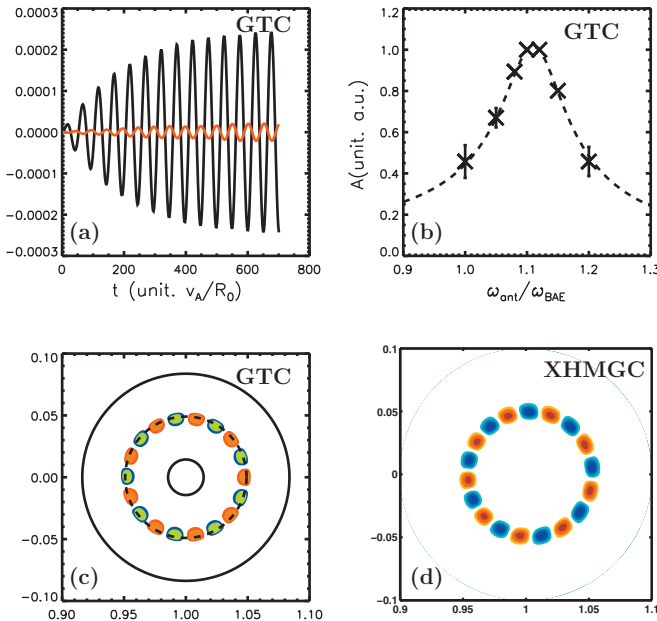


FIG. 4. (Color) BAE excitation by antenna. (a) Time evolution of the BAE real and imaginary parts in GTC simulation. (b) Saturated BAE amplitude vs antenna frequency. The dashed line is the numerical fitting by Eq. (18). (c) and (d) are the poloidal mode structure from GTC and xHMGC, respectively.

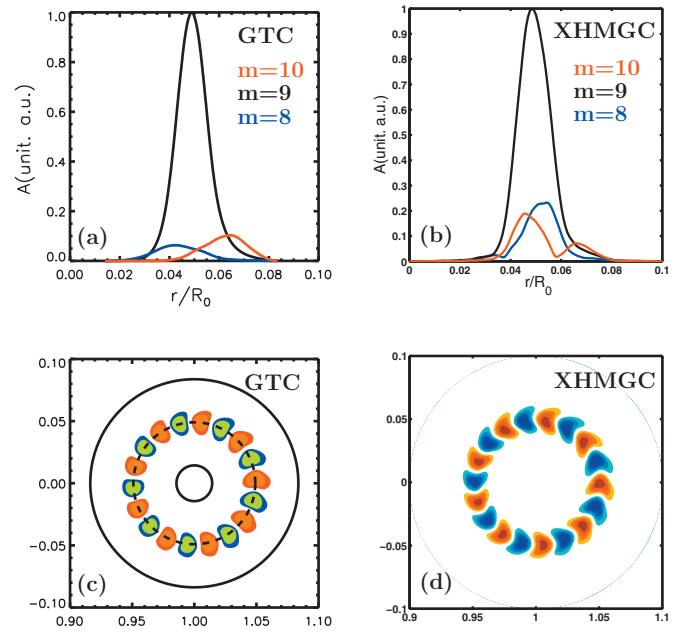


FIG. 5. (Color) BAE excitation by energetic particles. Radial (upper panels) and poloidal (lower panels) mode structures are shown. GTC and xHMGC results are on the left and right hand sides, respectively.

quency and damping rate are $1.47v_i/R_0$ and $-0.08v_i/R_0$, respectively. These results agree very well with the initial perturbation results in Sec. IV A and further verify the validity of the GTC gyrokinetic simulation of the BAE. Figures 4(c) and 4(d) are the antenna excited poloidal mode structures in GTC and xHMGC simulation, respectively. The mode structures from GTC and xHMGC agree with each other well and are quite similar to the initial perturbation simulation in Sec. IV A.

C. BAE excitation by energetic particles

In the energetic particle excitation simulation, we use $T_f=16T_i$ and $n_f=0.01n_0$. The maximum density gradient is $R/L_{nf} \approx 34$ and is located at the $\epsilon=0.05, q=3$ surface. Under these parameters, the BAE mode grows exponentially. The frequency and growth rate of the BAE are $\omega=1.42v_i/R_0$ and $\gamma=0.27v_i/R_0$ in GTC, while they are $\omega=1.55v_i/R_0$ and $\gamma=0.12v_i/R_0$ in xHMGC. Comparing with the initial and antenna cases, the frequency downshifts slightly in GTC while upshifts slightly in xHMGC. Figure 5 shows the excited BAE mode structures in the poloidal plane. The $(n=3, m=9)$ harmonic has a maximum amplitude at the $q=3$ mode rational surface. The radial structures of the dominant $m=9$ harmonic are almost the same between GTC and xHMGC, while the subdominant $m \pm 1$ harmonic structures are different. This may be due to the differences of the simulation geometry and equilibrium current in the two simulations. In GTC, the peak of the $m=10$ harmonic corresponds to the $q=10/3$ surface. Nonetheless, comparing Figs. 5(c) and 5(d), the poloidal mode structures of the two simulations are quite similar.

The convergence studies have also been done in the GTC simulations of the BAE excited by energetic particles. The scan of the number of grid points per wavelength N_g

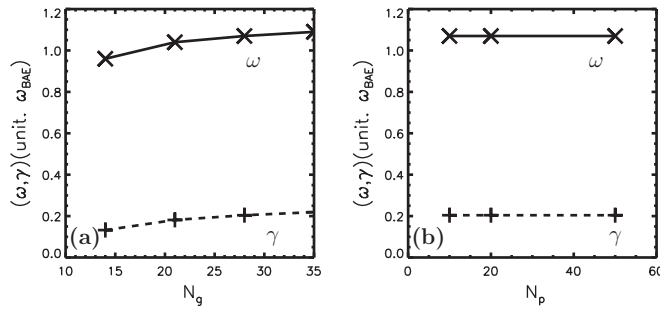


FIG. 6. (a) Scan of the number of grid points per wavelength N_g and (b) number of particles per cell N_p for the BAE frequency and growth rate in GTC simulations. Here, the energetic particle temperature and density ratio are kept unchanged, i.e., $T_f/T_i=16$, $n_f/n_i=0.01$. The solid line is the frequency ω and the dash line is the growth rate γ .

shows that both the real frequency and growth rate of the BAE grow as N_g increases and gradually converge [Fig. 6(a)]. Simulations with different number of particles per cell (N_p) show that the simulation results are not sensitive to the number of particles [Fig. 6(b)]. Based on these results, $N_g=28$ and $N_p=50$ are adequate for the BAE linear simulation.

In summary, the frequency and growth/damping rate comparisons between GTC and XHMGC are presented in Table I. We can see that the frequency of the initial perturbation simulation in the two codes agrees quite well. In the energetic particle excitation simulations, the GTC frequency is slightly smaller than the XHMGC frequency. The damping rate of the initial perturbation simulation agrees well with the antenna simulation in GTC. XHMGC has a larger damping rate than GTC in the initial perturbation simulations and the growth rate in GTC is larger than XHMGC in the energetic particle excitation simulations, possibly due to the numerical viscosity and resistivity in XHMGC and the differences in the equilibrium current and geometry.

V. SUMMARY

In this work, GTC is successfully used to study the BAE in toroidal plasmas. In our simulation, the BAE real frequency and damping rate measured in the initial perturbation simulation and in the antenna excitation simulation agree well with each other. The real frequency is slightly higher than the ideal MHD accumulation point frequency due to the kinetic effects of thermal ions. Simulations with energetic particle density gradient show exponential growth of BAE with a growth rate sensitive to the energetic particle temperature and density. The nonperturbative contributions by energetic particles modify the mode structure and reduce the fre-

TABLE I. Frequency and growth/damping rate comparisons between GTC and XHMGC.

Unit v_i/R_0	(ω, γ) in GTC	(ω, γ) in XHMGC
Initial perturbation	(1.47, -0.07)	(1.42, -0.15)
Antenna excitation	(1.47, -0.08)	
Energetic particle excitation	(1.42, 0.27)	(1.55, 0.12)

quency relative to the MHD theory. The finite Larmor radius effects of energetic particles reduce the BAE growth rate. Benchmarks between gyrokinetic particle simulation and hybrid MHD-gyrokinetic simulation show good agreement in BAE real frequency and mode structure.

ACKNOWLEDGMENTS

One of the authors (H.S.Z.) acknowledges useful discussions with L. Chen, W.J. Deng, and Z.X. Wang at UCI. This work was supported by the U.S. Department of Energy (DOE) SciDAC GSEP Center, the China Scholarship Council (Grant No. 2009601135), and National Basic Research Program of China (Grant Nos. 2008CB717803 and 2009GB105000).

- ¹C. Z. Cheng, L. Chen, and M. S. Chance, *Ann. Phys.* **161**, 21 (1985).
- ²W. W. Heidbrink, E. J. Strait, M. S. Chu, and A. D. Turnbull, *Phys. Rev. Lett.* **71**, 855 (1993).
- ³W. W. Heidbrink, E. Ruskov, E. M. Carolipio, J. Fang, M. A. Van Zeeland, and R. A. James, *Phys. Plasmas* **6**, 1147 (1999).
- ⁴A. D. Turnbull, E. J. Strait, W. W. Heidbrink, M. S. Chu, H. H. Duong, J. M. Greene, L. L. Lao, T. S. Taylor, and S. J. Thompson, *Phys. Fluids B* **5**, 2546 (1993).
- ⁵M. S. Chu, J. M. Greene, L. L. Lao, A. D. Turnbull, and M. S. Chance, *Phys. Fluids B* **4**, 3713 (1992).
- ⁶F. Zonca, L. Chen, and R. Santoro, *Plasma Phys. Controlled Fusion* **38**, 2011 (1996).
- ⁷F. Zonca, L. Chen, A. Botrugno, P. Buratti, A. Cardinali, R. Cesario, V. Pericoli Ridolfini, and JET-EFDA Contributors, *Nucl. Fusion* **49**, 085009 (2009).
- ⁸B. N. Breizman, M. S. Pekker, S. E. Sharapov, and JET-EFDA Contributors, *Phys. Plasmas* **12**, 112506 (2005).
- ⁹R. Nazikian, Z. Chang, E. D. Fredrickson, E. Mazzucato, S. H. Batha, R. Bell, R. Budny, C. E. Bush, C. Z. Cheng, A. Janos, F. Levinton, J. Manickam, D. K. Mansfield, H. K. Park, G. Rewoldt, S. Sabbagh, E. J. Synakowski, W. Tang, G. Taylor, and L. E. Zakharov, *Phys. Plasmas* **3**, 593 (1996).
- ¹⁰P. Buratti, P. Smeulders, F. Zonca, S. V. Annibaldi, M. De Benedetti, H. Kroegler, G. Regnoli, O. Tudisco, and the FTU Team, *Nucl. Fusion* **45**, 1446 (2005).
- ¹¹S. V. Annibaldi, F. Zonca, and P. Buratti, *Plasma Phys. Controlled Fusion* **49**, 475 (2007).
- ¹²O. Zimmermann, H. R. Koslowski, A. Kramer-Flecken, Y. Liang, R. Wolf, and the TEC Team, Proceedings of the 32nd EPS Conference on Plasma Physics, Tarragona, Spain, 2005, p. 4.059.
- ¹³W. Chen, J. Xiaoquan, Y. Qingwei, D. Xuantong, L. Yi, F. Beibin, H. Yuang, L. Wei, Z. Yan, Z. Jun, S. Xianming, L. Liancai, D. Xuru, and the HL-2A Team, *J. Phys. Soc. Jpn.* **79**, 044501 (2010).
- ¹⁴C. Nguyen, X. Garbet, R. Sabot, L.-G. Eriksson, M. Goniche, P. Maget, V. Basiuk, J. Decker, D. Elbeze, G. T. A. Huysmans, A. Macor, J.-L. Segui, and M. Schneider, *Plasma Phys. Controlled Fusion* **51**, 095002 (2009).
- ¹⁵S. T. Tsai and L. Chen, *Phys. Fluids B* **5**, 3284 (1993).
- ¹⁶S. Briguglio, C. Kar, F. Romanelli, G. Vlad, and F. Zonca, *Plasma Phys. Controlled Fusion* **37**, A279 (1995).
- ¹⁷C. Z. Cheng, N. N. Gorelenkov, and C. T. Hsu, *Nucl. Fusion* **35**, 1639 (1995).
- ¹⁸R. Santoro and L. Chen, *Phys. Plasmas* **3**, 2349 (1996).
- ¹⁹N. N. Gorelenkov and W. W. Heidbrink, *Nucl. Fusion* **42**, 150 (2002).
- ²⁰V. S. Marchenko and S. N. Reznik, *Nucl. Fusion* **49**, 022002 (2009).
- ²¹A. Bondeson and M. S. Chu, *Phys. Plasmas* **3**, 3013 (1996).
- ²²N. Winsor, J. L. Johnson, and J. M. Dawson, *Phys. Fluids* **11**, 2448 (1968).
- ²³C. Nguyen, X. Garbet, and A. I. Smolyakov, *Phys. Plasmas* **15**, 112502 (2008).
- ²⁴A. I. Smolyakov, C. Nguyen, and X. Garbet, *Nucl. Fusion* **50**, 054002 (2010).
- ²⁵P. Lauber, M. Brudgam, D. Curran, V. Igochine, K. Sassenberg, S. Gunter, M. Maraschek, M. Garcia-Munoz, N. Hicks, and the ASDEX Upgrade Team, *Plasma Phys. Controlled Fusion* **51**, 124009 (2009).

- ²⁶X. Wang, F. Zonca, and L. Chen, *Plasma Phys. Controlled Fusion* **52**, 115005 (2010).
- ²⁷Z. Lin, T. S. Hahm, W. W. Lee, W. M. Tang, and R. B. White, *Science* **281**, 1835 (1998).
- ²⁸I. Holod, W. L. Zhang, Y. Xiao, and Z. Lin, *Phys. Plasmas* **16**, 122307 (2009).
- ²⁹Y. Nishimura, *Phys. Plasmas* **16**, 030702 (2009).
- ³⁰W. J. Deng, Z. Lin, I. Holod, X. Wang, Y. Xiao, and W. L. Zhang, "Gyrokinetic particle simulations of reversed shear Alfvén eigenmode excited by antenna and fast ions," *Phys. Plasmas* (in press).
- ³¹H. S. Zhang, Z. Qiu, L. Chen, and Z. Lin, *Nucl. Fusion* **49**, 125009 (2009).
- ³²H. S. Zhang and Z. Lin, *Phys. Plasmas* **17**, 072502 (2010).
- ³³G. T. A. Huysmans, W. Kerner, D. Borba, H. A. Hoities, and J. P. Goedbloed, *Phys. Plasmas* **2**, 1605 (1995).
- ³⁴A. Fasoli, D. Borba, G. Bosia, D. J. Campbell, J. A. Dobbing, C. Gormezano, J. Jacquinet, P. Lavanchy, J. B. Lister, P. Marmillod, J.-M. Moret, A. Santagiustina, and S. Sharapov, *Phys. Rev. Lett.* **75**, 645 (1995).
- ³⁵A. Fasoli, D. Testa, T. Panis, A. Klein, J. A. Snipes, J. Sears, M. Gryaznevich, R. Martin, S. D. Pinches, and JET-EFDA Contributors, *Plasma Phys. Controlled Fusion* **52**, 075015 (2010).
- ³⁶S. Briguglio, F. Zonca, and G. Vlad, *Phys. Plasmas* **5**, 3287 (1998).
- ³⁷A. J. Brizard and T. S. Hahm, *Rev. Mod. Phys.* **79**, 421 (2007).
- ³⁸Y. Nishimura, Z. Lin, and W. X. Wang, *Phys. Plasmas* **14**, 042503 (2007).
- ³⁹Z. Lin and L. Chen, *Phys. Plasmas* **8**, 1447 (2001).
- ⁴⁰Z. Lin, Y. Nishimura, Y. Xiao, I. Holod, W. L. Zhang, and L. Chen, *Plasma Phys. Controlled Fusion* **49**, B163 (2007).
- ⁴¹W. W. Lee, *J. Comput. Phys.* **72**, 243 (1987).
- ⁴²Z. Lin and W. W. Lee, *Phys. Rev. E* **52**, 5646 (1995).
- ⁴³J. Harris, W. Benenson, and H. Stöcker, *Handbook of Physics*, edited by J. Harris, W. Benenson, and H. Stöcker (Springer, New York, 2002).